

Machine Learning Predicts Conversion and Molecular Weight Distributions in Computer Controlled Polymerization

Jin Da Tan^{1,2}, Balamurugan Ramalingam^{1,3}, Swee Liang Wong^{1,7}, Jayce Cheng¹, Yee-Fun Lim¹, Vijila Chellappan¹, Saif A. Khan^{2,4}, Jatin Kumar^{1,8}, Kedar Hippalgaonkar^{1,5,6}

Correspondence to kedar@ntu.edu.sg, jatinkumar@mac.com

¹ Institute of Materials Research & Engineering, Agency for Science Technology and Research, 2 Fusionopolis Way, 138634 Singapore

² National University of Singapore Graduate School – Integrative Sciences and Engineering Programme, 21 Lower Kent Ridge Road, Singapore 119077

³ Institute of Sustainability for Chemicals, Energy and Environment, Agency for Science Technology and Research, 8 Biomedical Grove, Singapore 138665

⁴ Department of Chemical and Biomolecular Engineering – National University of Singapore, 4 Engineering Drive 4, Singapore 117585

⁵ Department of Materials Science and Engineering, Nanyang Technological University, Singapore 639798

⁶ Institute of Functional Intelligent Materials – National University of Singapore, 4 Science Drive 2, Singapore 117544

⁷ Home Team Science and Technology Agency, Singapore 138507

⁸ Xinterra Pte. Ltd. 77 Robinson Road, Singapore 068896

Abstract

The skew and shape of the Molecular Weight Distribution (MWD) of polymers have a significant impact on polymer physical properties. Standard summary metrics statistically derived from the MWD only provide an incomplete picture of the polymer MWD. Machine learning (ML) methods coupled with high-throughput experimentation (HTE) could potentially allow for the prediction of the entire polymer MWD without information loss. In our work, we present a computer controlled HTE platform that is able to run up to 8 unique variable conditions for the free radical polymerizations of styrene. The segmented-flow HTE system was equipped with an inline Raman spectrometer and offline size exclusion chromatography (SEC) to obtain time dependent conversion and MWD respectively. In a supervised learning exercise, the gradient-boosted decision trees ML algorithm was used to predict monomer conversion from reagent concentrations and reaction time with high accuracy, using data obtained from the Raman spectra. A second ML algorithm uses the random forest regressor to predict entire MWDs of the synthesized polymer. Each algorithm can navigate the complexity of multiple parallel reactions occurring in a polymerization. The algorithm accurately predicts monomer conversion in the first case despite variations in the polymerization kinetic parameters over time. In the second case, we predict the polymer MWD where fine details such as the shape and skew of the MWD are captured without information loss. SHAP values were calculated to examine the dependence of the ML model output on the experimental conditions. A transfer learning approach was also used to enhance the predictive power of a Deep Neural Network (DNN) model in predicting batch polymerization MWDs. Overall, we demonstrate that the combination of HTE and ML provide a high level of predictive accuracy in determining polymerization outcomes, providing polymer chemists with the ability to target the synthesis of polymers with desired properties via the predicted conversion and MWD.

Introduction

An attribute of paramount importance in polymers is the molecular weight as it directly impacts material performance such as Young's modulus, viscosity and glass transition temperature.¹ The statistical nature of the polymerization process leads to a mixture of polymer chains with differing molecular weights, resulting in a molecular weight distribution (MWD).² The number-average molecular weight (M_n), weight-average molecular weight (M_w) and dispersity (\mathcal{D}) are important metrics used to characterize a polymer's MWD. While M_n , M_w and \mathcal{D} are widely used MWD descriptors, Gentekos and co-workers have reminded readers in a recent review that M_n , M_w and \mathcal{D} are inadequate descriptors of the MWD because they do not take into account the skew and shape of the MWD.³ Indeed, polymer samples can have very similar M_n , M_w and \mathcal{D} but have vastly different MWDs.⁴ Many have also discussed the downsides of using only dispersity to characterise the breadth of the polymer MWD, because \mathcal{D} is a relative measure of the breadth of the MWD and can only be used to compare polymer samples with similar M_n .^{5,6} One can conclude thus that these metrics overlook finer details found within the MWD of a polymer, which can significantly affect its properties.⁷ Moreover, while a polymer chemist may be able to target a particular M_n or \mathcal{D} through careful selection of synthesis parameters, targeting the full distribution during synthesis remains a difficult challenge. With the emergence of machine learning

(ML) methods, we posit that this challenge could be realized by predicting the full MWD based on input conditions, thereby adding another tool to the polymer chemists' toolbox.

ML methods have increasingly been incorporated into recent materials discovery research efforts^{8,9}, and range in its myriad applications from organic synthesis^{10–14}, to drug discovery^{15–17}, polymer design^{18–22} and many other areas^{23–27}, owing to their ability to dramatically speed up scientific discovery²⁸ and guide scientific experiments.²⁹ Coupled with the proliferation of ML in scientific research, computer-controlled platforms and automated workflows have also become increasingly prominent in scientific research.^{30,31} Automated platforms and high-throughput experimentation (HTE) accelerates data generation^{32,33}, which can boost the performance of data-hungry ML models.³⁴ The synergy between HTE and ML and their usage in scientific research brings about the potential to accelerate materials discovery and the significance of this trend cannot be overstated.^{35,36}

In polymer design, automation, HTE and ML have seen increased prominence. In recent work by Rubens et. al., an autonomous self-optimizing flow reactor coupled with size exclusion chromatography (SEC) was designed for the systematic targeting of polymer M_n , and this work demonstrates the elegance of combining automation with ML.³⁷ In another work by Zhou et. al., computer controlled syringe pumps were utilised to generate droplet flow, which allowed for the photopolymerization of monomers at high concentrations in a continuous flow setting, alleviating high viscosity and reactor clogging concerns.³⁸ Rizkin et. al. have combined automated microfluidic experimentation and ML to understand the reaction space and techno-economic outcomes of the coordination polymerization of 1-hexene.³⁹ In addition, conducting polymerizations in continuous flow reactors have been shown to be highly effective in promoting photoinduced polymerizations⁴⁰, allows easy access to block polymers^{41–43} and serves as an analytical tool in understanding polymerization kinetics.⁴⁴ The myriad advantages of polymerizations in flow reactors were summarized in an excellent review by Reis et. al.⁴⁵ The application of ML in polymer synthesis was exemplified by Houben et. al., where a multi objective active learner (MOAL) algorithm was developed and applied to the emulsion polymerization of a styrene and butyl acrylate two-monomer system to simultaneously target conversion and particle size in a closed-loop fashion.⁴⁶

The specific goal of engineering MWDs has been attempted through the method of accumulation of polymer samples with narrow MWDs synthesized via controlled polymerization techniques. This technique allows one to design and control the final MWD of the resultant polymer blend.^{47–51} Recently, the control of \bar{M} in aqueous ATRP has also been reported by Wang et al.⁵² While these are certainly important steps taken towards addressing the MWD design problem, it is not yet possible to predict the MWD as an outcome of a polymerization in a facile manner. Mathematical models have been used to describe the polymer MWD arising from free radical polymerizations,⁵³ however, these are highly complex with numerous assumptions. The use of HTE and ML in the study of polymer MWD, and specifically, free radical polymerization is unexplored. By formulating the study of the MWD as a multi-output

regression exercise, ML models can be trained to learn the mapping between input parameters and MWD in a simple and elegant way.

With this goal in mind, we developed a computer-controlled experimental platform combined with ML in the study of monomer conversion and polymer MWD for the thermally initiated polymerization of styrene. The setup allows us to increase experimental throughput via a segmented flow method, which allows for the screening of multiple experimental conditions at once. An inline Raman spectrometer downstream generates Raman spectra of the reaction mixture in real-time and is used to monitor the styrene conversion accurately at different residence times. Subsequently, an offline SEC measures the MWD of the polystyrene formed during the polymerization. Using a gradient-boosted decision trees ensemble ML model, we then predict styrene monomer conversion with good accuracy. We also trained a random forest ensemble ML model for the prediction of the entire polystyrene MWD. Unlike one-shot learning techniques that aim to make predictions given small datasets such as in low data drug discovery efforts⁵⁴, our HTE platform can generate experimental data at a higher throughput than traditional methods without compromising data quality. This allows us to leverage upon the power of the ML algorithms to make accurate predictions of relevant experimental targets. We hope that through the accurate prediction of monomer conversion and polymer MWD, our work could provide a case-study for polymer chemists on the benefits of incorporating ML and HTE into the polymer synthesis workflow, potentially allowing for the acceleration of novel polymeric materials discovery via targeting the synthesis of polymers with desired properties, guided by the predicted conversion and MWD.

Results and Discussion

A schematic representation of the computer-controlled segmented-flow platform is shown in Figure 1a. The platform consists of four independent syringe pump ports that were interfaced with a computer and controlled by the LabVIEW software. Three reagent syringes, comprising of styrene, *p*-xylene and AIBN dissolved in *p*-xylene were infused into a mixer using gas-tight syringes for efficient mixing of reagents, while the fourth syringe comprised of deionized and degassed water, used as an inert spacer. The aqueous and organic phases will be generated using a staggered infusion protocol – in a single step of infusion, syringe ports containing either organic reagents (styrene, *p*-xylene and AIBN dissolved in *p*-xylene) or aqueous reagent (deionized water) would infuse, but not both immiscible phases at the same time. A PTFE coil of pre-determined length was immersed in an oil bath at 85°C during polymerization. The outlet of the PTFE coil was passed through an inline Raman spectrometer for real-time spectra collection. A back pressure regulator (BPR) was connected as shown in Figure 1a to reduce pressure differences within the flow system to ensure uniform flow. A fraction collector was used to collect organic fractions for subsequent off-line SEC analysis. The water was dyed green to allow for better visual identification of the aqueous and organic phases during experimentation and fraction collection. The segmented-flow architecture (Figure 1b) was generated by alternating the infusion of organic reagents and water. After the segmented pattern of 9 different compositions (Figure 1b) were formed, water was infused as a carrier liquid at an appropriate flow rate to achieve the desired residence time. Specific experimental

setup details and operational procedures are included in the supporting information (SI). The vinyl peak trace was obtained by plotting the intensity of the vinyl peak against spectra index (Figure 1b) and clearly shows the individual organic segments which contain the styrene monomer. This setup allows for the compartmentalisation of reaction mixtures containing different stoichiometries of reagents simultaneously at a set bath temperature without cross-contamination and enhances experimental throughput.

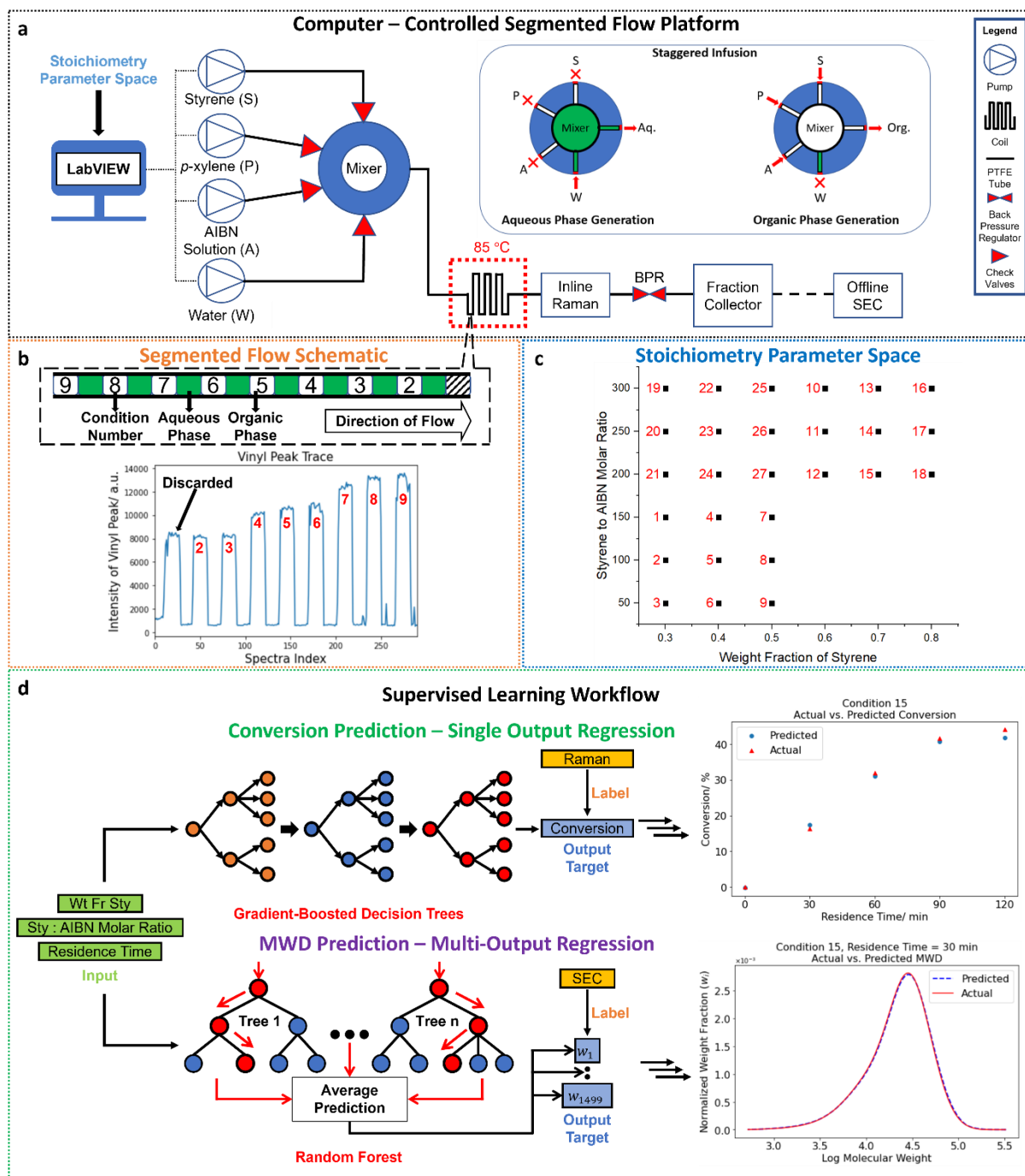


Figure 1. Computer-Controlled Segmented Flow Platform and Supervised Learning Workflow (a) Schematic of the computer-controlled segmented flow setup. Figure inset depicts a staggered infusion protocol for generating the organic and aqueous phases separately. (b) segmented flow schematic and the vinyl peak trace plot. The first condition of

each experiment is discarded. (c) stoichiometry parameter space showing weight fraction of styrene on the x-axis and styrene to AIBN molar ratio on the y-axis. Numbers highlighted in red indicate the label of the condition. (d) supervised learning workflow schematic for the prediction of monomer conversion and polymer MWD. Gradient-boosted decision trees were used for the prediction of conversion, while random forest was used for the prediction of MWD. The computer-controlled segmented flow platform allows for the generation of high-quality experimental data at a higher throughput than traditional methods, allowing for the training of ML models which can predict the monomer conversion and polymer MWD with high accuracy.

The design of experiment (DoE) constituted a uniform sampling of the parameter space of the experiment based on the input parameters of: (1) weight fraction of styrene in the organic phase; (2) the styrene to AIBN molar ratio and, (3) residence time of the reaction. Figure 1c shows the stoichiometry parameter space with the corresponding condition labels which was split into 4 quadrants with a single experiment running 9 conditions at once. The quadrant located at the bottom right was not tested on our platform due to the limits of AIBN solubility, resulting in the spontaneous precipitation of AIBN in the flow reactor. Styrene conversion and polystyrene MWD were determined for the uniformly sampled parameter space at residence times ranging from 0 min to 120 min at 30-minute intervals, with 0 min indicating no immersion of PTFE coil in the heated oil bath. Critically, our platform enables the parallel screening of 8 conditions, with the first condition discarded due to the syringe-pump driven flow not yet reaching steady state (details in the SI) and repeated in a subsequent segmented-flow experiment. The latter 8 conditions have different stoichiometries, which increases experimental throughput significantly over batch experiments. Importantly, an appropriate DoE coupled with HTE enables the rapid generation of reliable experimental data which can then be used for downstream data analytics and ML predictions.

The labelled dataset therefore consists of 3 input parameters, and the conversion and MWD outputs that we derived through the raw data obtained from the inline Raman spectrometer and the offline SEC, respectively. This data was used to perform the supervised learning tasks as shown in Figure 1d. The ML prediction exercise for conversion is a single-output regression problem as the target output conversion is a single scalar. However, the MWD target output is formulated as a multiple-output regression problem where the targeted output is the weight fraction vector containing the weight fractions of fixed molecular weights. This would allow the ML algorithm to model and predict the entire MWD of the polymer across a well-defined molecular weight range without information loss. Before training the ML algorithms on the labelled dataset, we arbitrarily chose Condition 15 as a validation condition for a final ML algorithm performance evaluation. The remaining labelled dataset was split into 80% training and 20% test sets. The experimental input features and output targets were scaled to range between 0 and 1. Hyperparameter tuning was conducted on the training set using 5-fold cross-validation (CV), and the ML algorithm was refit with the optimal hyperparameters and evaluated on the full training and test sets. Specific details on model training are included in the SI. As a final step of evaluation, we then use the best performing ML algorithms to predict the conversion and MWD of Condition 15 at different residence times and obtained highly accurate predictions ($R^2 > 0.99$, Figures 3e and 5i).

The inline Raman spectrometer collects Raman spectra in real-time during experimentation. Within a single Raman spectrum, we specifically monitored the area under the curve (AUC) of the Raman active vibrational modes of the styrene vinyl C=C stretch ($\sim 1630\text{ cm}^{-1}$)⁵⁵ and the *p*-xylene ring breathing mode ($\sim 830\text{ cm}^{-1}$)⁵⁶. Since Raman spectroscopy involves light scattering and absolute intensities cannot be used to quantify conversion⁵⁷, we normalized the vinyl AUC against the *p*-xylene AUC within a Raman spectrum to allow for the subsequent quantification of conversion across residence times. To allow for rapid data extraction from a large number of Raman spectra collected during the experiments, we automated the baseline subtraction, peak fitting, and AUC calculation processes via a Raman spectra parsing code written using Python and the entire workflow is summarized in Figure 2 below:

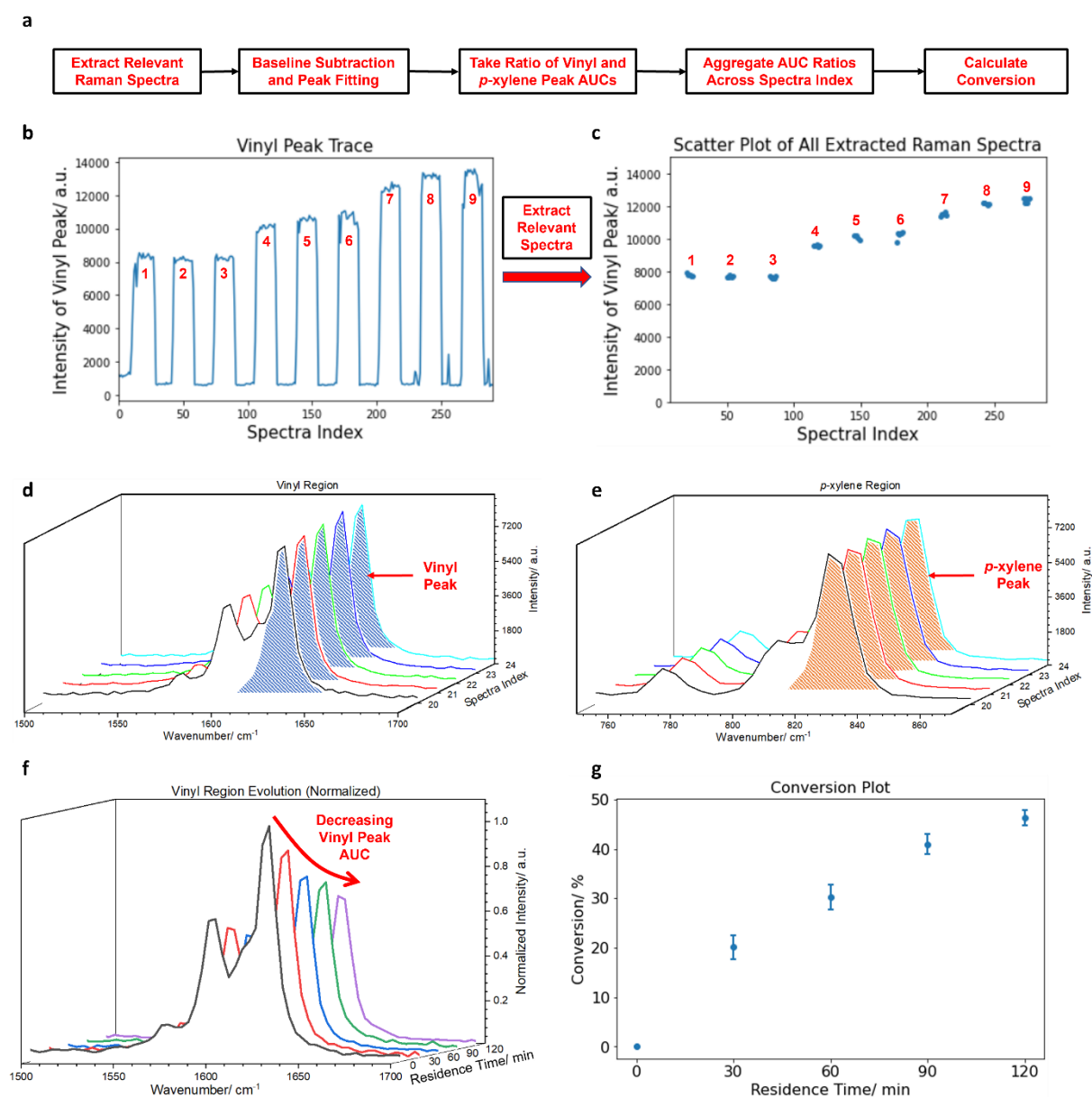


Figure 2. Monomer Conversion Calculation from Inline Raman Spectra Data (a) Workflow for calculation of conversion from the Raman spectra. (b, c) extraction of relevant Raman spectra from the vinyl peak trace (d) overlay of several Raman spectra of a single condition, featuring the styrene vinyl region (vinyl peak AUC is highlighted in blue). (e) overlay

of several Raman spectra of a single condition, featuring the *p*-xylene region (*p*-xylene peak AUC is highlighted in orange). (f) waterfall plot depicting the decrease in the vinyl peak AUC over time. (g) a representative conversion plot shows an increasing conversion with residence time. The data parsing code allows for the rapid quantification of monomer conversion across residence times for multiple conditions at once, owing to its ability to automate the baseline subtraction, peak fitting, and AUC calculation processes for a large number of Raman spectra.

The first step of data processing involves the extraction of the relevant Raman spectra containing the vinyl peak associated with its respective condition label, taking reference from the vinyl peak trace as shown in Figures 2b and 2c. Each dot in Figure 2c represents a Raman spectrum containing the vinyl peak from a particular condition. After extracting the relevant Raman spectra for each condition, the vinyl and *p*-xylene regions were first subjected to a baseline correction, followed by a curve fitting of the line-shape of the peaks using a linear combination of Lorentzian functional forms with the python package *lmfit*.⁵⁸ The AUC of all relevant peaks can then be derived in an automated fashion via an iterative loop for all extracted Raman spectra. Figures 2d and 2e shows the vinyl and *p*-xylene regions for 5 representative Raman spectra of a single condition. Relevant peak AUCs are highlighted for clarity. The *p*-xylene peak AUC is then divided (normalized) against the vinyl peak AUC to obtain an AUC ratio. This ratio is aggregated across the 5 spectra of a single condition to obtain a mean and standard deviation of the ratio. The conversion is calculated via the following equation:

$$\text{Conversion (\%)} = \left(1 - \frac{R_t}{R_0}\right) \times 100\%$$

where R_0 is the mean ratio at residence time of 0 min (no reaction) and R_t is the mean ratio at residence time of t min. The corresponding standard deviations were propagated during conversion calculation to obtain the error for each conversion value. An evolution of the normalized vinyl AUC over time is shown in Figure 2f. A decrease in the normalized vinyl AUC indicates an increase in monomer conversion over time. A plot of conversion values against residence time is shown in Figure 2g. We have verified that the conversion obtained from this approach agrees well with the conversion derived from NMR studies. Specific details on the Raman peak assignments, data parsing code and NMR studies are included in the SI.

Once the Raman data was parsed and conversion data collected, ML algorithms were trained to map the relationship between styrene conversion and the input parameters. We approached this regression problem by first training and tuning the hyperparameters of different ML models on the training data. Figure 3a shows the performance of various ML algorithms on conversion as measured by the root mean squared error (RMSE). The hyperparameters for the respective ML Algorithms were tuned prior to evaluation using grid and random search methods. Linear ML models (Lasso, Elastic Net, Linear, Ridge) were unable to capture the non-linear relationship between the input features and the output target conversion and hence perform poorly as indicated by both metrics. The K-nearest neighbours and decision tree ML algorithms severely overfitted the training set as shown in Figure 3a with RMSE values of 0 for the training set, but non-zero RMSE for the test set. This implies that the trained K-nearest neighbours and decision tree ML models are not generalizable to previously

unseen conversion data in the context of this study. They were therefore not used for the final evaluation on condition 15. Between support vector regression, random forest, and gradient-boosted decision trees, the lattermost ML algorithm performed the best with the lowest test set RMSE of 0.038. Furthermore, a training set RMSE of 0.035 indicates that the ML model was not overfitting the training set as the training scores were close to the test scores. Therefore, the gradient-boosted decision trees ML model was the best choice for mapping the input parameters to conversion without overfitting to the training set and being generalizable to test set examples previously unseen, striking a good balance between the bias and variance of the ML model.⁵⁹ To visualize the robustness of the ML model predictions, a plot of predicted versus actual conversion values is shown in Figure 3d. Training and test set values close to the diagonal line indicate a good model fit onto the data and a high predictive accuracy of the ML model, respectively. As a final step of model evaluation, the gradient-boosted decision trees ML model was used to predict the conversion of condition 15 across five residence times, which it had not been previously trained on. Figure 3e shows the actual vs. predicted conversion plots for condition 15 and the R^2 value of 0.9936 obtained shows that the ML algorithm has accurately predicted the conversion for condition 15 across all residence times. Python code used for ML model training and conversion prediction are included in the SI.

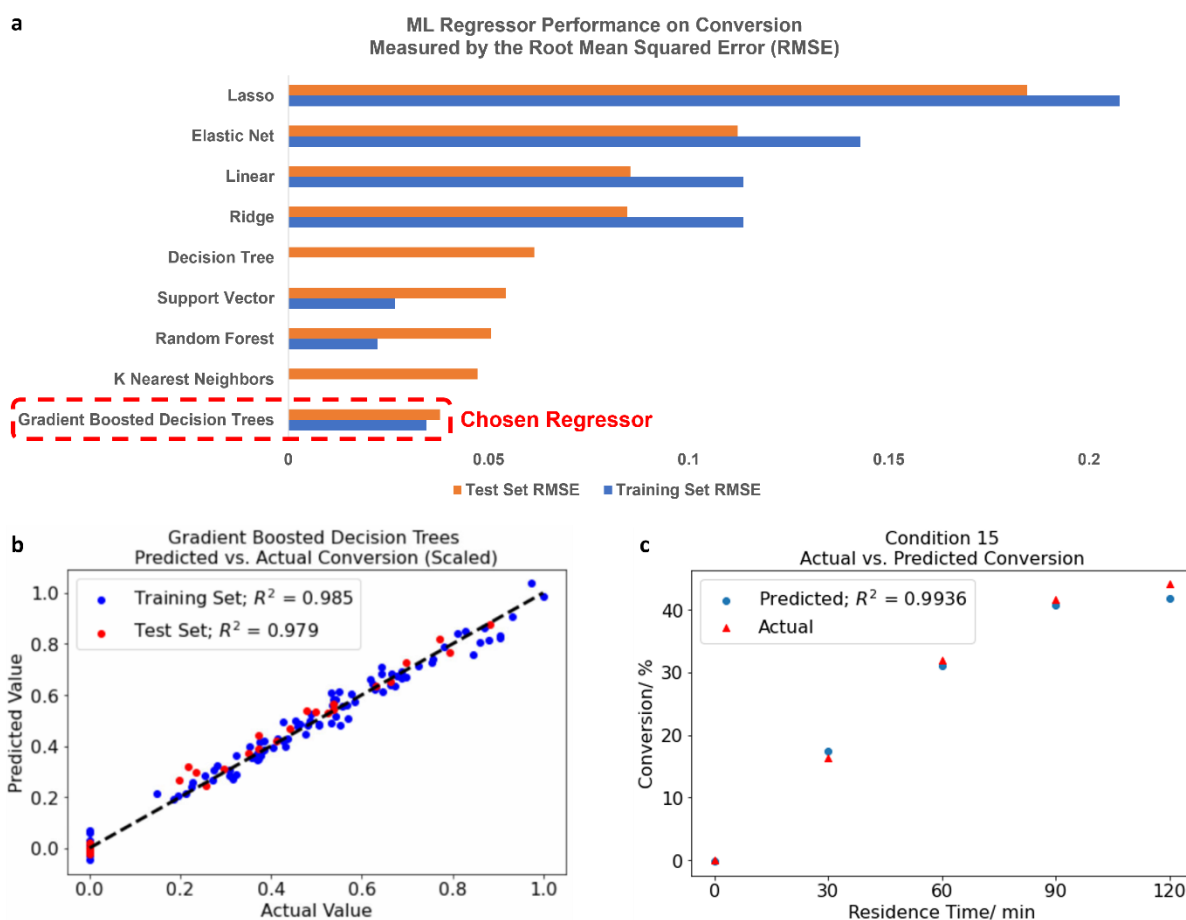


Figure 3. ML Model Selection and Prediction of Conversion (a) ML regressor performance on conversion measured by the RMSE. Regressors were arranged in order of decreasing test set RMSE. The gradient-boosted decision trees regressor was chosen as for

conversion prediction. (b) Predicted value versus actual value plot of the gradient-boosted decision trees ML algorithm on the training and test sets. (c) Plot of experimental and predicted conversion plots for condition 15. The goodness of fit (R^2) between actual and predicted conversions across all residence times is above 0.99, indicating a very accurate prediction by the gradient-boosted decision trees ML model.

Since the monomer conversion is closely related to the kinetics of polymerization, we further investigate the relationship between styrene conversion and free-radical polymerization kinetics in the context of this study. The instantaneous rate of monomer disappearance, or the instantaneous rate of polymerization, R_p , shown in the equation below, is linearly dependent on the monomer concentration^{2,60}:

$$R_p = -\frac{d[M]}{dt} = k_p[M] \left(\frac{fk_d[I]}{k_t} \right)^{1/2}$$

In the equation, $[M]$ is the monomer concentration, $[I]$ is the initiator concentration, f is the initiator efficiency, k_p is the propagation rate constant of the monomer, k_d is the decomposition rate constant of the initiator and k_t is the termination rate constant. This was derived from the mechanism of a free radical initiated chain polymerization assuming steady-state as well as equal reactivity with respect to the propagating radical size.^{2,60} The linear relationship between R_p and $[M]$ only holds if the steady-state and equal reactivity conditions are met and that the polymerization interval under study is sufficiently short such that kinetic parameters in the above equation do not change meaningfully within the interval. We expect the aforementioned parameters to vary during the polymerization process in the relatively long residence time intervals of our study. Firstly, f is known to change with differing monomer concentrations.^{61,62} Termination and propagation rate constants are also influenced by the radical length⁶³, viscosity^{64–66}, as well as variations in the mass transport of propagating radical moieties.^{67–69} $[I]$ changes over time as the initiator gradually dissociates into primary radicals. Standard polymer kinetic rate plots of our experiments (details in the SI) show that the kinetics of radical polymerization are observed to deviate from a straight line, confirming that a single linear relationship does not hold over the course of our experiments. This also explains the inability of linear ML models to accurately predict conversion across residence times in our study. Nevertheless, based on the high degree of accuracy of the predicted conversions by the non-linear gradient boosted decision trees model, we are able to conclude that the non-linear ML model can accurately capture the variations in kinetic parameters of an uncontrolled free radical polymerization across all residence times tested during the experiment.

Now that we have investigated the kinetics leading to the conversion, the next part of the campaign involves the study of polymer MWDs. To achieve this, organic segments from the segmented flow setup were manually collected into separate vials, diluted with THF and subjected to SEC analysis without further purification. The SEC was first calibrated using polystyrene standards with narrow MWDs and the mapping between the molecular weights and retention volume provided by the standard calibration was used for subsequent MWD extraction from the chromatogram.

The formulation of an ML problem statement for the MWD is non-trivial. While MWD descriptors like M_n , M_w and \bar{D} used individually as targets for ML prediction, information on the skew and the shape of the MWD are still absent within the summary metrics.³ The direct prediction of the entire MWD using ML models, without information loss, would be far more powerful and descriptive of the polymerization outcome. Therefore, a well-defined MWD target for the ML algorithm was integral to the success of the supervised learning task. We approached the ML problem statement by framing it as a multi-output regression problem, where the target of ML prediction is a vector with a fixed number of components, containing the weight fractions of the polymer fraction of a particular molecular weight. A vector output with a fixed number of components requires the systematic extraction of the MWD within a well-defined retention volume window for all chromatograms. Figure 4 shows the MWD extraction process in detail:

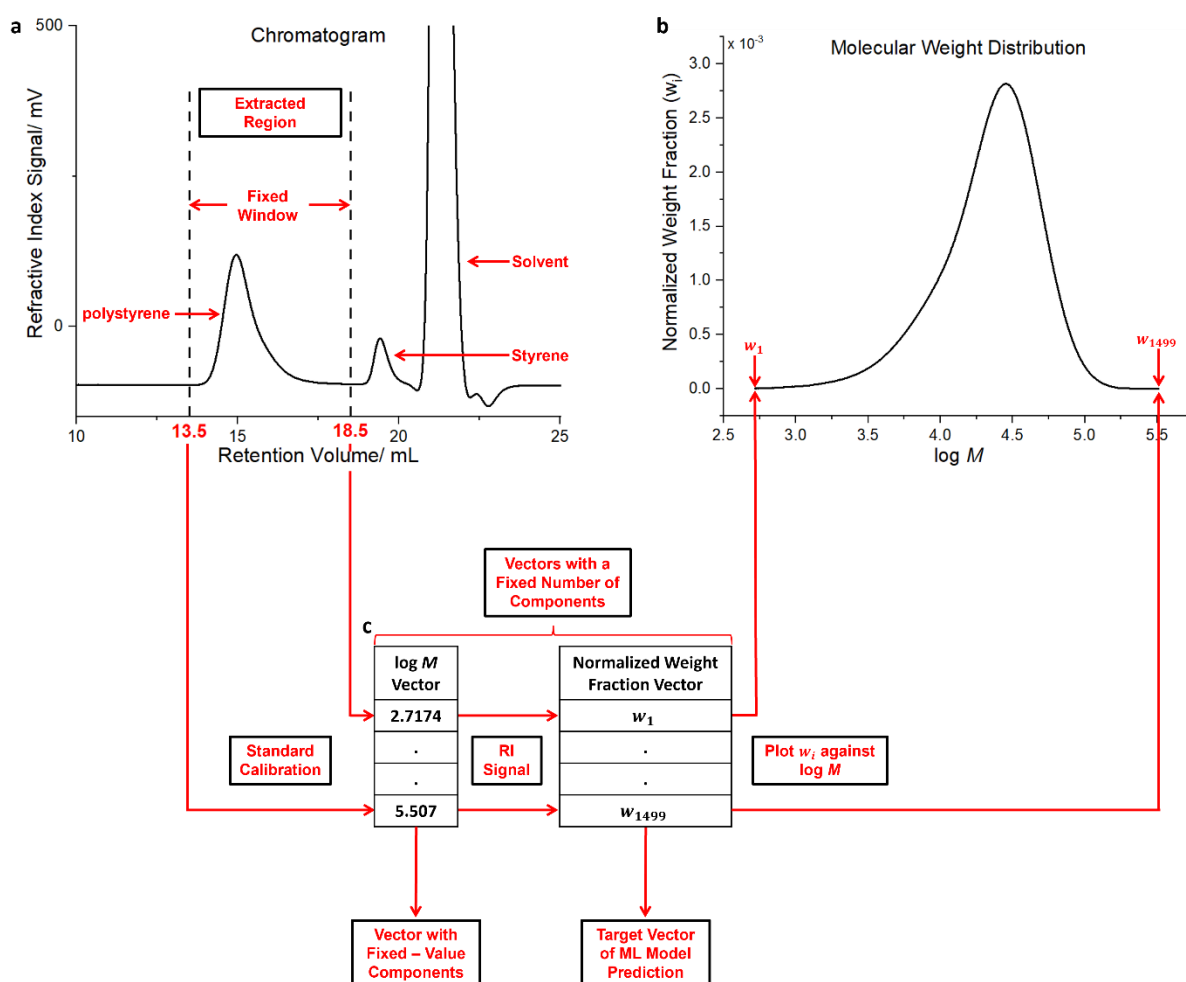


Figure 4. MWD Target Vector Extraction Methodology (a) Extraction of the polystyrene peak from the SEC chromatogram within a fixed window of retention volume. (b) representative MWD extracted from the chromatogram within the fixed retention volume window. (c) the extracted $\log M$ and the extracted normalized weight fraction vectors both have a fixed number of components (1499 components) due to the extraction of the polystyrene peak within a fixed retention volume window. The $\log M$ vector contains $\log M$ values which are fixed, owing to the standard calibration used throughout all extractions, while

the normalized weight fraction vector contains normalized weight fraction values which depends on the refractive index (RI) signal obtained from the detector on the SEC. The resultant MWD weight fraction vector which describes the entire polystyrene MWD fully without information loss was used as the target for ML prediction and this MWD target vector extraction methodology can be applied for chromatograms obtained from SECs with the same standard calibration and operating parameters.

Figure 4a shows a representative chromatogram with the relevant polystyrene, styrene and solvent peaks labelled. MWD data of the polystyrene was extracted within a fixed extraction window of retention volume from 13.5 mL to 18.5 mL. The resultant MWD is shown in Figure 4b, with the normalized weight fraction (w_i) on the y-axis plotted against the log molecular weight ($\log M$) on the x-axis. Figure 4c shows the connection between Figure 4a and 4b where extraction of the polystyrene peak within a fixed retention volume window of the chromatogram ensures that the $\log M$ vector has a fixed number of 1499 components. A further consequence of the standard calibration is that the $\log M$ vector has components with fixed values as the standard calibration procedure maps retention volumes to $\log M$ values using polystyrene standards with narrow MWDs. The corresponding weight fraction vector determined by the refractive index (RI) signal will also have 1499 components. The weight fraction values within the weight fraction vector were normalized to sum to 1 and the weight fraction vector which describes the entire polystyrene MWD fully without information loss was used as the target for ML prediction. Furthermore, by representing the entire MWD as a vector, multimodal MWDs or MWDs with irregular shapes can be fully represented, and common MWD descriptors of M_n , M_w and \bar{D} or higher moments of the MWD such as skewness and kurtosis³ can be subsequently derived if information loss can be tolerated.

ML models were trained to tackle a multi-output regression problem to learn the mapping from the input parameters to the output vector containing 1499 components comprising of the normalized weight fractions. In an approach similar to the conversion predictions, data for condition 15 were chosen for the final model evaluation. Figure 5a shows the performance of various ML algorithms on the normalized weight fraction vector as measured by the RMSE. For multiple output regression models, the metrics were calculated element wise and averaged across all components. The hyperparameters for the respective ML Algorithms were tuned prior to evaluation. Linear ML models (Lasso, Elastic Net, Linear and Ridge) performed poorly due to the poor linear fit of the input features to the target vector. K nearest neighbours and decision tree ML models overfitted the training set with RMSE values of 0 for the training set, but non-zero RMSE for the test set and were not generalizable towards unseen MWD data. Between random forest and deep neural network (DNN) ML models, while the DNN had a lower RMSE of 0.046 compared to the random forest model (RMSE = 0.047), the random forest model achieved the best balance between bias and variance by having a larger training set RMSE of 0.018, compared to the DNN's training set RMSE of 0.009, indicating that the random forest model is less likely to overfit than the DNN model and was chosen for MWD prediction. Finally, the random forest ML model was used to predict the conversion of condition 15 across four residence times. Figure 5b shows the experimental MWD and the predicted MWD of condition 15 at a residence time of 30 minute. Figure 5c shows the overlay of

experimental MWD across different residence times, while Figure 5d highlights the ability of the ML model to recognise the gradual and subtle shift of the MWD towards higher molecular weights. An R^2 value higher than 0.99 was obtained for all predictions and it shows the robustness of the random forest ML algorithm in this multiple output regression exercise. The Python code used for ML model training and MWD prediction are included in the SI.

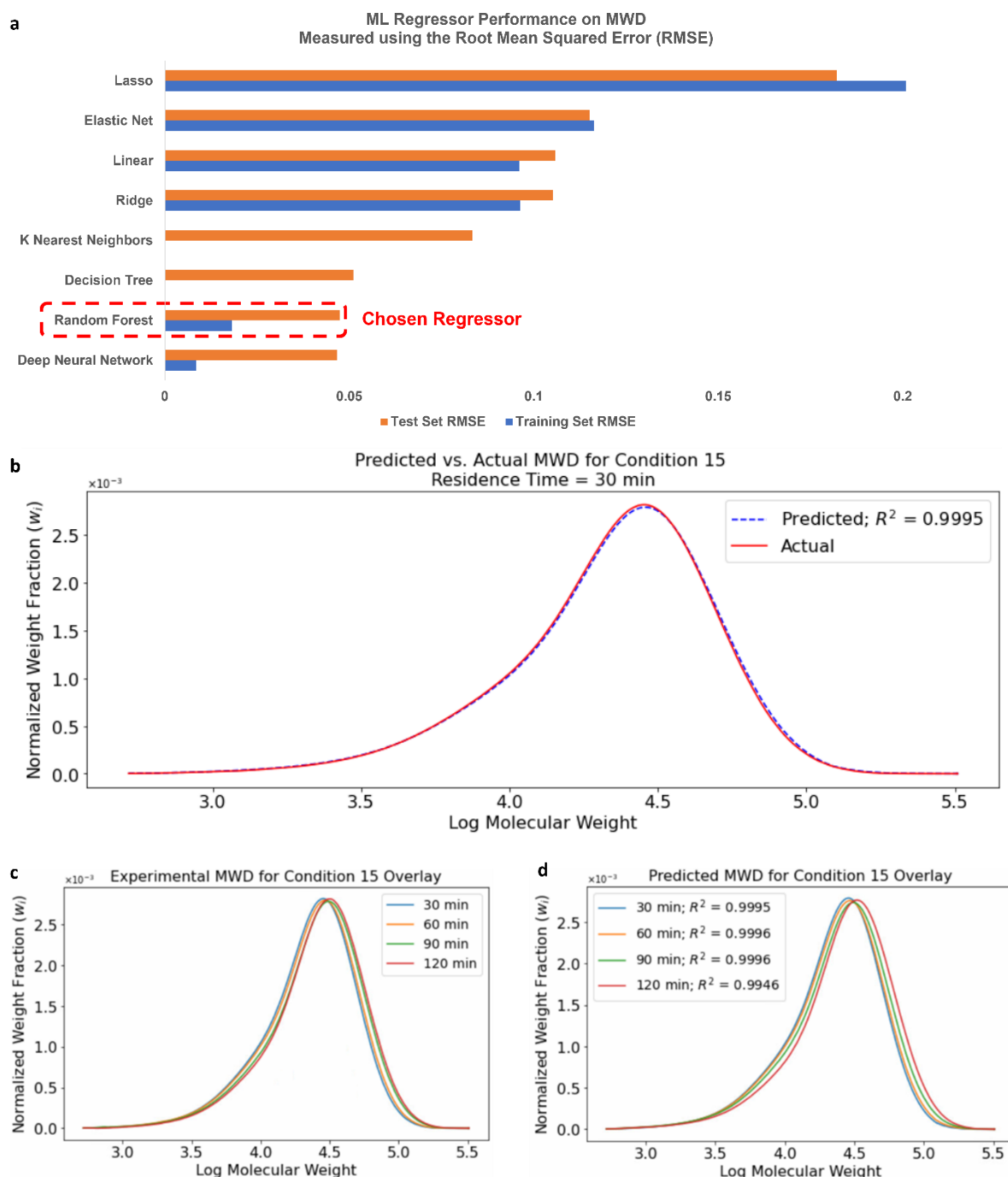


Figure 5. ML Model Selection and Multi-Output Regression for MWD Prediction (a) ML regressor performance on conversion measured by the RMSE. Regressors were arranged in order of decreasing test set RMSE. The random forest regressor was chosen for MWD prediction. (b) plot of experimental and predicted MWD for condition 15 at a residence time of 30 min with an R^2 value of 0.9995. (c, d) overlay of experimental and predicted MWDs at

different residence times for condition 15, respectively. The random forest model can predict the MWD for condition 15 at all residence times with very good accuracy: the goodness of fit (R^2) between the actual and predicted MWD at a given residence time above 0.99 and the high degree of accuracy of the MWD predictions indicate the robustness of the random forest ML algorithm in tackling the multiple output regression problem, allowing for the accurate prediction of polymer MWDs without information loss.

The data presented in Figure 5 shows that the random forest algorithm can not only predict MWDs with very high accuracy, but it also captures the finer details of the MWD, such as the skew of the MWDs of condition 15 which gives a low molecular weight tail, as well as the evolution of the MWD with reaction time, without information loss. From a machine learning standpoint, we showcase the ability of our multi-output regressor to learn from the experimental data, linking process conditions to a target vector that represents the MWD. Mechanistically, the ML regressor was able to, once again, capture the nuances of the MWD that result from complex mechanistic events that occur during a free radical polymerization process, which can be difficult to express numerically whether through the typical MWD descriptors of M_n , M_w and \mathcal{D} , or even through the asymmetry factor (A_s) of an MWD.³

To better understand the impact of the input features on the conversion and MWD outputs, we calculated the SHAP (SHapley Additive exPlanations) values of features to understand how the features influence the output of the ML model. SHAP values are measures of feature importance and represent a feature's responsibility for a change in the model output and they are calculated via a game theoretic approach.⁷⁰ While calculating the SHAP values for conversion would give us an idea of how the input features affect the conversion, calculating the SHAP values for the MWD vector would not be highly illuminating, as each element of the 1499-dimension output vector would be related to a feature by the SHAP value. Such granular detail would not be useful in understanding how the features affect the shape and skew of the MWD. Therefore, in addition to the conversion, we concatenated the summary statistics of each MWD (namely M_n , M_w , \mathcal{D} , M_z , M_p and A_s) into a vector and used this 7-dimensional vector as the output of a DNN model. The model can then be trained in the same way as previously described, and the SHAP values can be calculated to enhance model interpretability and understand the feature-output relationship. Figure 6a shows the architecture of the DNN trained on the training data, with 3 nodes in the input layer representing the features, 7 hidden layers of 32 nodes, and 7 nodes in the output layer for the 7-dimension output vector. The SHAP values for all features were plotted in bee swarm plots, where each dot in its corresponding feature row represents its relative impact on a particular instance of the output as indicated by the location of the dot on the x-axis representing the SHAP value. More information on the hyperparameter tuning of the DNN and SHAP value calculation is included in the SI.

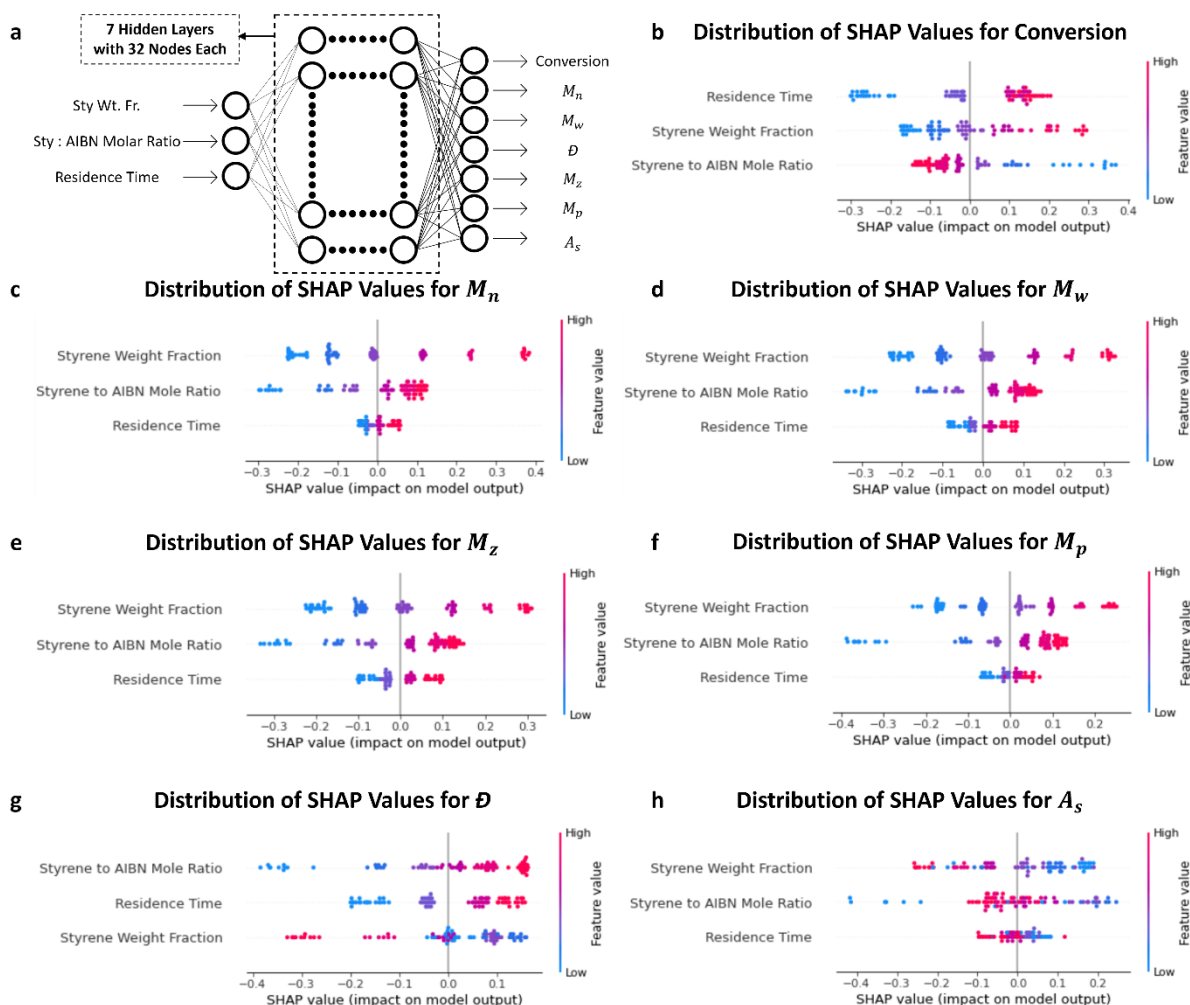


Figure 6. SHAP Values Toward ML Interpretability for Conversion and MWD Summary Metrics. (a) DNN architecture trained using the training set and used for subsequent SHAP values calculation. (b-h) Distribution of feature SHAP Values for conversion, M_n , M_w , M_z , M_p , \bar{D} and A_s , respectively. The colormap represents the magnitude of the feature value. (b) shows that low residence times led to a negative impact on the conversion, while low styrene to AIBN molar ratio led to a positive impact on the conversion. (c-f) distribution of feature SHAP values for M_n , M_w , M_z and M_p respectively, where a low styrene weight fraction and low styrene to AIBN molar ratio had a negative impact on the output, while the residence time had relatively minor impact. (g) shows that high styrene weight fractions and low styrene to AIBN mole ratios had a negative impact on \bar{D} . (h) shows that low styrene to AIBN mole ratios had a negative impact on the A_s while the residence time had relatively minor impact.

The SHAP values help to reinforce our understanding of how the features affects the output and helps illuminate the underlying chemical rationale that drives the relationship. For instance, low residence times led to lower conversion, as less styrene molecules would be converted to polystyrene in a shorter time. Similarly, high styrene weight fractions would lead to higher M_n , M_w , M_z and M_p as more styrene molecules are present to form polystyrenes of higher molecular weights. Conversely, low styrene to AIBN molar ratios would lead to polystyrenes of lower average molecular weights because there are less styrene molecules per AIBN molecule available to add to the growing kinetic chain on average. Low styrene to AIBN molar ratios also led to lower

dispersities because of the lower average molecular weights of the polystyrenes which set an upper bound to the range of molecular weights the polystyrenes could have, limiting the range of molecular weights and the relative breadth of the MWD the polystyrene would possess. This also results in lower A_s as the resultant MWD becomes more symmetric about the M_p . More information on the calculation of A_s is included in the SI. It is also not surprising that residence times would have a limited impact on the average molecular weight of polystyrenes because high molecular weight polymers are formed very quickly initially in chain growth polymerizations and the average molecular weight of the polymer does not change dramatically throughout the course the reaction, unlike the situation of step-growth polymerizations. Evidently, SHAP values are powerful tools in understanding the underlying kinetics of the reaction, as described by the ML model.

Next, we use transfer learning⁷⁴ to circumvent the limitations of the flow setup, going beyond the limitations of AIBN solubility (shown as the inaccessible bottom-right quadrant in Figure 1c). We randomly chose 3 conditions in this region to be run on batch reactors and measured the resultant polystyrene's MWDs at 30-minute intervals. While we were running the same reaction in different reactors, the mass and heat transfer characteristics would differ between a flow and batch reactor.⁷¹⁻⁷³ The transfer learning process involves fine-tuning a previously trained DNN model. Figure 7a shows the stoichiometry parameter space where a DNN pre-trained on the conditions run on the flow system (annotated in red) was fine-tuned using the training examples from the bottom right quadrant (annotated in blue). Figure 7b shows a schematic of the transfer learning process, where the weights for the first two hidden layers learnt previously were frozen (pre-training), while the weights for the output layer was allowed to be trained (fine-tuning) using new training examples from the batch reactions. The output vector from the DNN was further processed via the Savitzky-Golay filter and re-normalization to give the final predicted MWD. A comparison was made between the previously high performing random forest model and the fine-tuned DNN to highlight the difference in the model performances. Figures 7c and 7d highlights the difference in predictive power of the ML models. More information on the transfer learning process and the comparison of predictive accuracy between the DNN model with and without fine-tuning is included in the SI.

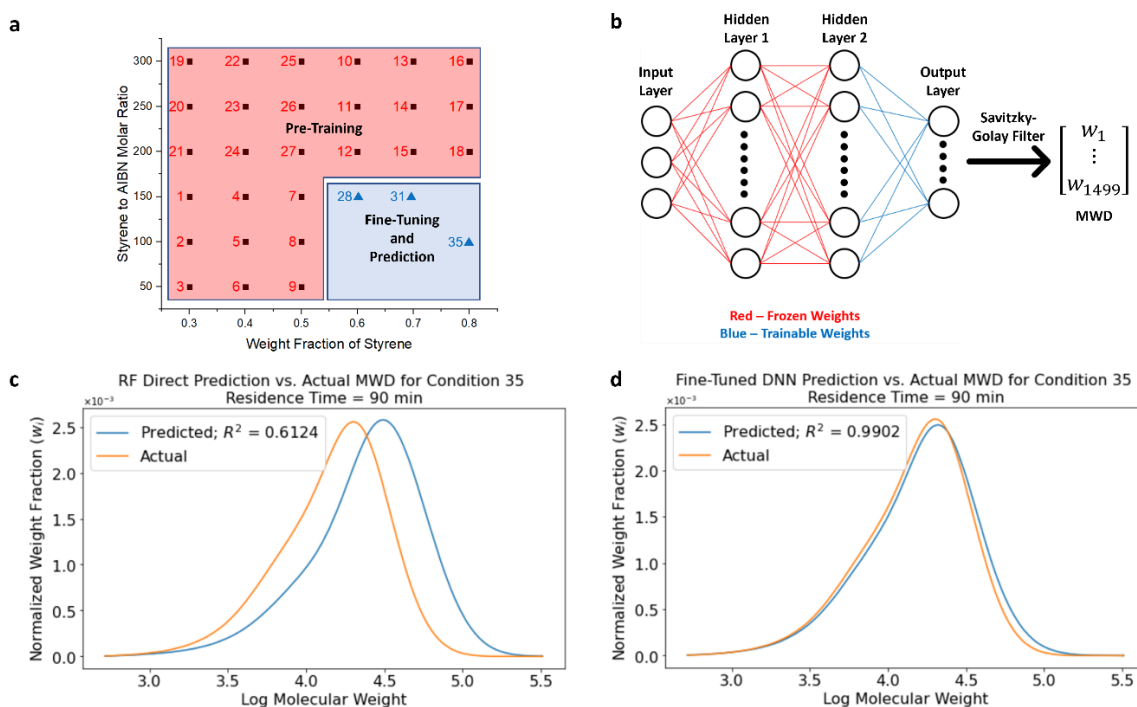


Figure 7. Transfer Learning Improves ML Predictive Power in a Related Domain (a) stoichiometry parameter space where the previous conditions run in flow were used to pre-train the DNN (red region), while the new conditions run in batch were used to fine-tune the DNN (blue region) (b) schematic of the fine-tuning of a DNN for transfer learning, where frozen weights in the first two layers are highlighted in red, and the trainable weights at the last layer are highlighted in blue. A Savitzky-Golay filter was used to smoothen the output from the DNN to give the final predicted MWD. (c) plot of experimental versus random forest predicted MWD for condition 35 at a residence time of 90 min with a moderate R^2 value of 0.6124. (d) plot of experimental versus fine-tuned DNN predicted MWD for condition 35 at a residence time of 90 min with a relatively higher R^2 value of 0.9902. Transfer learning allows for the transfer of knowledge from one domain (polymerization in flow reactors) to a related domain (polymerization in batch reactors), improving the predictive power of the ML model.

We have shown that the transfer learning approach works well in enhancing the predictive prowess of an ML algorithm, and the fine-tuning process requires dramatically less amount of data as compared to pre-training the DNN. In effect, while we utilised 83 data points from the flow reactor to pretrain the DNN, we only used 3 data points from the batch reactor to fine-tune the DNN. Through the transfer learning approach, we could extend the knowledge from high throughput flow experiments to batch experiments with far fewer data points. We believe that this transfer learning approach can be applied in other instances, where a HTE platform can be used to generate a large amount of data in a more accessible region of the input parameter space to pre-train a DNN, which can then be fine-tuned with data from a less accessible region of the input parameter space which might require more laborious, stringent low-throughput experimental procedures, to generate more accurate predictions.

Conclusions

In this work, we have outlined an approach towards accurately predicting outcomes of the thermal-initiated radical polymerization of styrene using a combination of HTE,

automated data analysis and ML. Our high throughput segmented flow platform was able to conduct multiple compartmentalized polymerization reactions in parallel, with the collection of *in situ* Raman spectroscopic data and sample collection for offline SEC. Automated data analysis allowed for the rapid determination of monomer conversion, while the systematic MWD target vector extraction methodology which results in a complete representation of the MWD proved essential for the success of the MWD prediction exercise. We expect these methods to be applicable to similar workflows which might involve other monomers or types of polymerizations.

The parallelization of experiments, combined with automated data analysis affords a platform that can generate large amounts of high-quality experimental data which are essential for training accurate ML algorithms. A gradient-boosted decision tree ML algorithm was able to accurately predict monomer conversion as a function of reagent stoichiometry and reaction time for both training and test data, as well as unseen data in the form of one masked condition. Our model was able to learn the kinetics of the polymerization without being explicitly programmed to do so. We also demonstrate that with a careful ML problem statement formulation, proper predictive target definition and MWD extraction methodology, a random forest regressor was similarly able to accurately predict the entire polymer MWD across residence times. Our predictions were accurate in capturing the nuances of a MWD, including features such as its shape and skew, without information loss. This approach is unprecedented as there have not been any reported methods that can accurately represent and more interestingly, predict an entire MWD from reaction conditions. In addition, we calculated SHAP values to better understand the relationship between the input and the ML model output. We also applied a transfer learning approach for the prediction of polymer MWD run in batch, via the fine-tuning of a pre-trained DNN, achieving good accuracies in the process. The implications and potential directions for this platform are twofold. Firstly, with our high throughput platform coupled with automated data analysis, we were able to generate polymerization data at an accelerated pace. This would potentially enable large scale studies to look at polymerization kinetics, especially of complex systems with many variables such as other reagents and temperatures. Secondly, the ability of the ML models in navigating the complexity of multiple parallel ongoing elementary reactions within the radical polymerization mechanism could be leveraged in investigating poorly understood monomers, or more complex polymerizations such as co- or ter-polymerizations.

References

- (1) Swallowe, G. M. *Tensile and Compressive Testing*, 1st ed.; Springer Netherlands, 1999.
- (2) Odian, G. *Principles of Polymerization*, 4th ed.; John Wiley & Sons, Ltd, 2004.
- (3) Gentekos, D. T.; Sifri, R. J.; Fors, B. P. Controlling Polymer Properties through the Shape of the Molecular-Weight Distribution. *Nat. Rev. Mater.* **2019**, *4* (12), 761–774. <https://doi.org/10.1038/s41578-019-0138-8>.
- (4) Kottisch, V.; Gentekos, D. T.; Fors, B. P. “Shaping” the Future of Molecular Weight Distributions in Anionic Polymerization. *ACS Macro Lett.* **2016**, *5* (7), 796–800. <https://doi.org/10.1021/acsmacrolett.6b00392>.

- (5) Harrisson, S. The Downside of Dispersity: Why the Standard Deviation Is a Better Measure of Dispersion in Precision Polymerization. *Polym. Chem.* **2018**, 9 (12), 1366–1370. <https://doi.org/10.1039/c8py00138c>.
- (6) Rane, S. S.; Choi, P. Polydispersity Index: How Accurately Does It Measure the Breadth of the Molecular Weight Distribution? *Chem. Mater.* **2005**, 17 (4), 926. <https://doi.org/10.1021/cm048594i>.
- (7) Nadgorny, M.; Gentekos, D. T.; Xiao, Z.; Singleton, S. P.; Fors, B. P.; Connal, L. A. Manipulation of Molecular Weight Distribution Shape as a New Strategy to Control Processing Parameters. *Macromol. Rapid Commun.* **2017**, 38 (19), 1700352. <https://doi.org/10.1002/marc.201700352>.
- (8) Jackson, N. E.; Webb, M. A.; de Pablo, J. J. Recent Advances in Machine Learning towards Multiscale Soft Materials Design. *Curr. Opin. Chem. Eng.* **2019**, 23, 106–114. <https://doi.org/10.1016/j.coche.2019.03.005>.
- (9) Butler, K. T.; Davies, D. W.; Cartwright, H.; Isayev, O.; Walsh, A. Machine Learning for Molecular and Materials Science. *Nature* **2018**, 559 (7715), 547–555. <https://doi.org/10.1038/s41586-018-0337-2>.
- (10) Coley, C. W.; Thomas, D. A.; Lummiss, J. A. M.; Jaworski, J. N.; Breen, C. P.; Schultz, V.; Hart, T.; Fishman, J. S.; Rogers, L.; Gao, H.; Hicklin, R. W.; Plehiers, P. P.; Byington, J.; Piotti, J. S.; Green, W. H.; Hart, A. J.; Jamison, T. F.; Jensen, K. F. A Robotic Platform for Flow Synthesis of Organic Compounds Informed by AI Planning. *Science (80-.)*. **2019**, 365 (6453), eaax1566. <https://doi.org/10.1126/science.aax1566>.
- (11) Segler, M. H. S.; Preuss, M.; Waller, M. P. Planning Chemical Syntheses with Deep Neural Networks and Symbolic AI. *Nature* **2018**, 555 (7698), 604–610. <https://doi.org/10.1038/nature25978>.
- (12) de Almeida, A. F.; Moreira, R.; Rodrigues, T. Synthetic Organic Chemistry Driven by Artificial Intelligence. *Nat. Rev. Chem.* **2019**, 3 (10), 589–604. <https://doi.org/10.1038/s41570-019-0124-0>.
- (13) Reid, J. P.; Sigman, M. S. Holistic Prediction of Enantioselectivity in Asymmetric Catalysis. *Nature* **2019**, 571 (7765), 343–348. <https://doi.org/10.1038/s41586-019-1384-z>.
- (14) Jorner, K.; Tomberg, A.; Bauer, C.; Sköld, C.; Norrby, P.-O. Organic Reactivity from Mechanism to Machine Learning. *Nat. Rev. Chem.* **2021**, 5 (4), 240–255. <https://doi.org/10.1038/s41570-021-00260-x>.
- (15) Segler, M. H. S.; Kogej, T.; Tyrchan, C.; Waller, M. P. Generating Focused Molecule Libraries for Drug Discovery with Recurrent Neural Networks. *ACS Cent. Sci.* **2018**, 4 (1), 120–131. <https://doi.org/10.1021/acscentsci.7b00512>.
- (16) Jiménez-Luna, J.; Grisoni, F.; Schneider, G. Drug Discovery with Explainable Artificial Intelligence. *Nat. Mach. Intell.* **2020**, 2 (10), 573–584. <https://doi.org/10.1038/s42256-020-00236-4>.
- (17) Kadurin, A.; Nikolenko, S.; Khrabrov, K.; Aliper, A.; Zhavoronkov, A. DruGAN: An Advanced Generative Adversarial Autoencoder Model for de Novo Generation of New Molecules with Desired Molecular Properties in Silico. *Mol.*

- Pharm.* **2017**, *14* (9), 3098–3104.
<https://doi.org/10.1021/acs.molpharmaceut.7b00346>.
- (18) Mannodi-Kanakkithodi, A.; Chandrasekaran, A.; Kim, C.; Huan, T. D.; Pilania, G.; Botu, V.; Ramprasad, R. Scoping the Polymer Genome: A Roadmap for Rational Polymer Dielectrics Design and Beyond. *Mater. Today* **2018**, *21* (7), 785–796. <https://doi.org/10.1016/j.mattod.2017.11.021>.
- (19) Kim, C.; Chandrasekaran, A.; Huan, T. D.; Das, D.; Ramprasad, R. Polymer Genome: A Data-Powered Polymer Informatics Platform for Property Predictions. *J. Phys. Chem. C* **2018**, *122* (31), 17575–17585.
<https://doi.org/10.1021/acs.jpcc.8b02913>.
- (20) Jha, A.; Chandrasekaran, A.; Kim, C.; Ramprasad, R. Impact of Dataset Uncertainties on Machine Learning Model Predictions: The Example of Polymer Glass Transition Temperatures. *Model. Simul. Mater. Sci. Eng.* **2019**, *27* (2), 024002. <https://doi.org/10.1088/1361-651X/aaf8ca>.
- (21) Kumar, J. N.; Li, Q.; Tang, K. Y. T.; Buonassisi, T.; Gonzalez-Oyarce, A. L.; Ye, J. Machine Learning Enables Polymer Cloud-Point Engineering via Inverse Design. *npj Comput. Mater.* **2019**, *5* (1), 1–6. <https://doi.org/10.1038/s41524-019-0209-9>.
- (22) Mannodi-Kanakkithodi, A.; Pilania, G.; Huan, T. D.; Lookman, T.; Ramprasad, R. Machine Learning Strategy for Accelerated Design of Polymer Dielectrics. *Sci. Rep.* **2016**, *6* (1), 1–10. <https://doi.org/10.1038/srep20952>.
- (23) Yang, K. K.; Wu, Z.; Arnold, F. H. Machine-Learning-Guided Directed Evolution for Protein Engineering. *Nat. Methods* **2019**, *16* (8), 687–694.
<https://doi.org/10.1038/s41592-019-0496-6>.
- (24) Ruiz Euler, H.-C.; Boon, M. N.; Wildeboer, J. T.; van de Ven, B.; Chen, T.; Broersma, H.; Bobbert, P. A.; van der Wiel, W. G. A Deep-Learning Approach to Realizing Functionality in Nanoelectronic Devices. *Nat. Nanotechnol.* **2020**, *15* (12), 992–998. <https://doi.org/10.1038/s41565-020-00779-y>.
- (25) Raissi, M.; Yazdani, A.; Karniadakis, G. E. Hidden Fluid Mechanics: Learning Velocity and Pressure Fields from Flow Visualizations. *Science (80-.)*. **2020**, *367* (6481), 1026–1030. <https://doi.org/10.1126/science.aaw4741>.
- (26) Bash, D.; Cai, Y.; Chellappan, V.; Wong, S. L.; Yang, X.; Kumar, P.; Tan, J. Da; Abutaha, A.; Cheng, J. J.; Lim, Y.; Tian, S. I. P.; Ren, Z.; Mekki-Berrada, F.; Wong, W. K.; Xie, J.; Kumar, J.; Khan, S. A.; Li, Q.; Buonassisi, T.; Hippalgaonkar, K. Multi-Fidelity High-Throughput Optimization of Electrical Conductivity in P3HT-CNT Composites. *Adv. Funct. Mater.* **2021**, 2102606.
<https://doi.org/10.1002/adfm.202102606>.
- (27) Mekki-Berrada, F.; Ren, Z.; Huang, T.; Wong, W. K.; Zheng, F.; Xie, J.; Tian, I. P. S.; Jayavelu, S.; Mahfoud, Z.; Bash, D.; Hippalgaonkar, K.; Khan, S.; Buonassisi, T.; Li, Q.; Wang, X. Two-Step Machine Learning Enables Optimized Nanoparticle Synthesis. *npj Comput. Mater.* **2021**, *7* (1), 1–10.
<https://doi.org/10.1038/s41524-021-00520-w>.
- (28) Schmidt, J.; Marques, M. R. G.; Botti, S.; Marques, M. A. L. Recent Advances and Applications of Machine Learning in Solid-State Materials Science. *npj*

- Comput. Mater.* **2019**, 5 (1), 1–36. <https://doi.org/10.1038/s41524-019-0221-0>.
- (29) Rohr, B.; Stein, H. S.; Guevarra, D.; Wang, Y.; Haber, J. A.; Aykol, M.; Suram, S. K.; Gregoire, J. M. Benchmarking the Acceleration of Materials Discovery by Sequential Learning. *Chem. Sci.* **2020**, 11 (10), 2696–2706. <https://doi.org/10.1039/c9sc05999g>.
- (30) Mateos, C.; Nieves-Remacha, M. J.; Rincón, J. A. Automated Platforms for Reaction Self-Optimization in Flow. *React. Chem. Eng.* **2019**, 4 (9), 1536–1544. <https://doi.org/10.1039/c9re00116f>.
- (31) Clayton, A. D.; Schweidtmann, A. M.; Clemens, G.; Manson, J. A.; Taylor, C. J.; Niño, C. G.; Chamberlain, T. W.; Kapur, N.; Blacker, A. J.; Lapkin, A. A.; Bourne, R. A. Automated Self-Optimisation of Multi-Step Reaction and Separation Processes Using Machine Learning. *Chem. Eng. J.* **2020**, 384, 123340. <https://doi.org/10.1016/j.cej.2019.123340>.
- (32) Selekman, J. A.; Qiu, J.; Tran, K.; Stevens, J.; Rosso, V.; Simmons, E.; Xiao, Y.; Janey, J. High-Throughput Automation in Chemical Process Development. *Annu. Rev. Chem. Biomol. Eng.* **2017**, 8 (1), 525–547. <https://doi.org/10.1146/annurev-chembioeng-060816-101411>.
- (33) Kumar, J. N.; Li, Q.; Jun, Y. Challenges and Opportunities of Polymer Design with Machine Learning and High Throughput Experimentation. *MRS Commun.* **2019**, 9 (2), 537–544. <https://doi.org/10.1557/mrc.2019.54>.
- (34) Banko, M.; Brill, E. Scaling to Very Very Large Corpora for Natural Language Disambiguation. In *Proceedings of the 39th Annual Meeting on Association for Computational Linguistics*; Association for Computational Linguistics (ACL): Toulouse, France, 2001; pp 26–33. <https://doi.org/10.3115/1073012.1073017>.
- (35) Tabor, D. P.; Roch, L. M.; Saikin, S. K.; Kreisbeck, C.; Sheberla, D.; Montoya, J. H.; Dwaraknath, S.; Aykol, M.; Ortiz, C.; Tribukait, H.; Amador-Bedolla, C.; Brabec, C. J.; Maruyama, B.; Persson, K. A.; Aspuru-Guzik, A. Accelerating the Discovery of Materials for Clean Energy in the Era of Smart Automation. *Nat. Rev. Mater.* **2018**, 3 (5), 5–20. <https://doi.org/10.1038/s41578-018-0005-z>.
- (36) Correa-Baena, J. P.; Hippalgaonkar, K.; van Duren, J.; Jaffer, S.; Chandrasekhar, V. R.; Stevanovic, V.; Wadia, C.; Guha, S.; Buonassisi, T. Accelerating Materials Development via Automation, Machine Learning, and High-Performance Computing. *Joule* **2018**, 2 (8), 1410–1420. <https://doi.org/10.1016/j.joule.2018.05.009>.
- (37) Rubens, M.; Vrijsen, J. H.; Laun, J.; Junkers, T. Precise Polymer Synthesis by Autonomous Self-Optimizing Flow Reactors. *Angew. Chemie - Int. Ed.* **2019**, 58 (10), 3183–3187.
- (38) Zhou, Y.; Gu, Y.; Jiang, K.; Chen, M. Droplet-Flow Photopolymerization Aided by Computer: Overcoming the Challenges of Viscosity and Facilitating the Generation of Copolymer Libraries. *Macromolecules* **2019**, 52 (15), 5611–5617. <https://doi.org/10.1021/acs.macromol.9b00846>.
- (39) Rizkin, B. A.; Shkolnik, A. S.; Ferraro, N. J.; Hartman, R. L. Combining Automated Microfluidic Experimentation with Machine Learning for Efficient Polymerization Design. *Nat. Mach. Intell.* **2020**, 2 (2), 200–209.

<https://doi.org/10.1038/s42256-020-0166-5>.

- (40) Cole, J. P.; Federico, C. R.; Lim, C. H.; Miyake, G. M. Photoinduced Organocatalyzed Atom Transfer Radical Polymerization Using Continuous Flow. *Macromolecules* **2019**, *52* (2), 747–754. <https://doi.org/10.1021/acs.macromol.8b02688>.
- (41) Chen, M.; Johnson, J. A. Improving Photo-Controlled Living Radical Polymerization from Trithiocarbonates through the Use of Continuous-Flow Techniques. *Chem. Commun.* **2015**, *51* (31), 6742–6745. <https://doi.org/10.1039/c5cc01562f>.
- (42) Vandenberg, J.; De Moraes Ogawa, T.; Junkers, T. Precision Synthesis of Acrylate Multiblock Copolymers from Consecutive Microreactor RAFT Polymerizations. *J. Polym. Sci. Part A Polym. Chem.* **2013**, *51* (11), 2366–2374. <https://doi.org/10.1002/pola.26593>.
- (43) Lauterbach, F.; Rubens, M.; Abetz, V.; Junkers, T. Ultrafast PhotoRAFT Block Copolymerization of Isoprene and Styrene Facilitated through Continuous-Flow Operation. *Angew. Chemie Int. Ed.* **2018**, *57* (43), 14260–14264. <https://doi.org/10.1002/anie.201809759>.
- (44) Reis, M. H.; Davidson, C. L. G.; Leibfarth, F. A. Continuous-Flow Chemistry for the Determination of Comonomer Reactivity Ratios. *Polym. Chem.* **2018**, *9* (13), 1728–1734. <https://doi.org/10.1039/c7py01938f>.
- (45) Reis, M. H.; Leibfarth, F. A.; Pitet, L. M. Polymerizations in Continuous Flow: Recent Advances in the Synthesis of Diverse Polymeric Materials. *ACS Macro Lett.* **2020**, *9* (1), 123–133. <https://doi.org/10.1021/acsmacrolett.9b00933>.
- (46) Houben, C.; Peremezhney, N.; Zubov, A.; Kosek, J.; Lapkin, A. A. Closed-Loop Multitarget Optimization for Discovery of New Emulsion Polymerization Recipes. *Org. Process Res. Dev.* **2015**, *19* (8), 1049–1053. <https://doi.org/10.1021/acs.oprd.5b00210>.
- (47) Walsh, D. J.; Schinski, D. A.; Schneider, R. A.; Guironnet, D. General Route to Design Polymer Molecular Weight Distributions through Flow Chemistry. *Nat. Commun.* **2020**, *11* (1), 1–9. <https://doi.org/10.1038/s41467-020-16874-6>.
- (48) Rubens, M.; Junkers, T. Comprehensive Control over Molecular Weight Distributions through Automated Polymerizations. *Polym. Chem.* **2019**, *10* (46), 6315–6323. <https://doi.org/10.1039/c9py01013k>.
- (49) Junkers, T.; Vrijsen, J. H. Designing Molecular Weight Distributions of Arbitrary Shape with Selectable Average Molecular Weight and Dispersity. *Eur. Polym. J.* **2020**, *134*, 109834. <https://doi.org/10.1016/j.eurpolymj.2020.109834>.
- (50) Corrigan, N.; Almasri, A.; Taillades, W.; Xu, J.; Boyer, C. Controlling Molecular Weight Distributions through Photoinduced Flow Polymerization. *Macromolecules* **2017**, *50* (21), 8438–8448. <https://doi.org/10.1021/acs.macromol.7b01890>.
- (51) Corrigan, N.; Manahan, R.; Lew, Z. T.; Yeow, J.; Xu, J.; Boyer, C. Copolymers with Controlled Molecular Weight Distributions and Compositional Gradients through Flow Polymerization. *Macromolecules* **2018**, *51* (12), 4553–4563.

<https://doi.org/10.1021/acs.macromol.8b00673>.

- (52) Wang, H. S.; Parkatzidis, K.; Harrisson, S.; Truong, N. P.; Anastasaki, A. Controlling Dispersity in Aqueous Atom Transfer Radical Polymerization: Rapid and Quantitative Synthesis of One-Pot Block Copolymers. *Chem. Sci.* **2021**, *12* (43), 14376–14382. <https://doi.org/10.1039/d1sc04241f>.
- (53) Clay, P. A.; Gilbert, R. G. Molecular Weight Distributions in Free-Radical Polymerizations. 1. Model Development and Implications for Data Interpretation. *Macromolecules* **1995**, *28* (2), 552–569. <https://doi.org/10.1021/ma00106a021>.
- (54) Altae-Tran, H.; Ramsundar, B.; Pappu, A. S.; Pande, V. Low Data Drug Discovery with One-Shot Learning. *ACS Cent. Sci.* **2017**, *3* (4), 283–293. <https://doi.org/10.1021/acscentsci.6b00367>.
- (55) Noda, L. K.; Sala, O. Resonance Raman Investigation on the Interaction of Styrene and 4-Methyl Styrene Oligomers on Sulphated Titanium Oxide. *Spectrochim. Acta - Part A Mol. Biomol. Spectrosc.* **2000**, *56* (1), 145–155. [https://doi.org/10.1016/S1386-1425\(99\)00128-6](https://doi.org/10.1016/S1386-1425(99)00128-6).
- (56) Bai, Y.; Yu, Z.; Liu, R.; Li, N.; Yan, S.; Yang, K.; Liu, B.; Wei, D.; Wang, L. Pressure-Induced Crystallization and Phase Transformation of Para-Xylene. *Sci. Rep.* **2017**, *7* (1), 1–10. <https://doi.org/10.1038/s41598-017-05639-9>.
- (57) Van Den Brink, M.; Hansen, J.-F. O.; De Peinder, P.; Van Herk, A. M.; German, A. L. Measurement of Partial Conversions During the Solution Copolymerization of Styrene and Butyl Acrylate Using On-Line Raman Spectroscopy. *J. Appl. Polym. Sci.* **2000**, *79* (3), 426–436. [https://doi.org/10.1002/1097-4628\(20010118\)79:3<426::AID-APP50>3.0.CO;2-V](https://doi.org/10.1002/1097-4628(20010118)79:3<426::AID-APP50>3.0.CO;2-V).
- (58) Newville, M.; Otten, R.; Nelson, A.; Ingargiola, A.; Stensitzki, T.; Allan, D.; Fox, A.; Carter, F.; Michał; Pustakhod, D.; Ineuhaus; Weigand, S.; Osborn, R.; Glenn; Deil, C.; Mark; Hansen, A. L. R.; Pasquevich, G.; Foks, L.; Zobrist, N.; Frost, O.; Beelen, A.; Stuermer; kwertyops; Polloreno, A.; Caldwell, S.; Almarza, A.; Persaud, A.; Gamari, B.; Maier, B. F. Lmfit/Lmfit-Py 1.0.2. February 7, 2021. <https://doi.org/doi.org/10.5281/zenodo.4516651>.
- (59) Friedman, J.; Hastie, T.; Tibshirani, R. *The Elements of Statistical Learning Data Mining, Interface and Prediction*; 2009.
- (60) Flory, P. J. *Principles of Polymer Chemistry*; Cornell University Press, 1953.
- (61) Buback, M.; Frauendorf, H.; Günzler, F.; Huff, F.; Vana, P. Determining Initiator Efficiency in Radical Polymerization by Electrospray-Ionization Mass Spectrometry. *Macromol. Chem. Phys.* **2009**, *210* (19), 1591–1599. <https://doi.org/10.1002/macp.200900237>.
- (62) Bevington, J. C. The Sensitized Polymerization of Styrene: The Rate and Efficiency of Initiation. *Trans. Faraday Soc.* **1955**, *51* (0), 1392–1397. <https://doi.org/10.1039/TF9555101392>.
- (63) Gridnev, A. A.; Ittel, S. D. Dependence of Free-Radical Propagation Rate Constants on the Degree of Polymerization. *Macromolecules* **1996**, *29* (18),

- 5864–5874. <https://doi.org/10.1021/ma960422m>.
- (64) Fenyvesi, G.; Nagy, A.; Foldes-Berezsnich, T.; Tudos, F. Kinetics of Radical Polymerization. III. Kinetic Investigation of Styrene Polymerization in Viscous Medium. *J. Macromol. Sci. Part A - Chem.* **1990**, *27* (5), 637–647. <https://doi.org/10.1080/00222339009349648>.
- (65) Brooks, B. W. Viscosity Effects in the Free-Radical Polymerization of Methyl Methacrylate. *Proc R Soc London Ser A* **1977**, *357* (1689), 183–192. <https://doi.org/10.1098/rspa.1977.0162>.
- (66) Cioffi, M.; Hoffmann, A. C.; Janssen, L. P. B. M. Reducing the Gel Effect in Free Radical Polymerization. *Chem. Eng. Sci.* **2001**, *56* (3), 911–915. [https://doi.org/10.1016/S0009-2509\(00\)00305-5](https://doi.org/10.1016/S0009-2509(00)00305-5).
- (67) Barner-Kowollik, C.; Russell, G. T. Chain-Length-Dependent Termination in Radical Polymerization: Subtle Revolution in Tackling a Long-Standing Challenge. *Prog. Polym. Sci.* **2009**, *34* (11), 1211–1259. <https://doi.org/10.1016/j.progpolymsci.2009.07.002>.
- (68) Lovestead, T. M.; Theis, A.; Davis, T. P.; Stenzel, M. H.; Barner-Kowollik, C. Accessing the Chain Length Dependence of the Termination Rate Coefficient for Disparate Length Radicals via Reversible Addition Fragmentation Chain Transfer Chemistry: A Theoretical Study. *Macromolecules* **2006**, *39* (15), 4975–4982. <https://doi.org/10.1021/ma060646x>.
- (69) Ito, K. Evaluation of Termination Rate by Segmental and Translational Diffusions in Radical Polymerizations. *Polym. J.* **1979**, *11* (10), 795–803. <https://doi.org/10.1295/polymj.11.795>.
- (70) Lundberg, S. M.; Lee, S.-I. A Unified Approach to Interpreting Model Predictions. In *31st Conference on Neural Information Processing Systems (NIPS 2017)*; Long Beach, CA, USA, 2017.
- (71) Noël, T.; Cao, Y.; Laudadio, G. The Fundamentals behind the Use of Flow Reactors in Electrochemistry. *Acc. Chem. Res.* **2019**, *52* (10), 2858–2869. https://doi.org/10.1021/ACS.ACCOUNTS.9B00412/ASSET/IMAGES/LARGE/R9B00412_0010.JPEG.
- (72) Webb, D.; Jamison, T. F. Continuous Flow Multi-Step Organic Synthesis. *Chem. Sci.* **2010**, *1* (6), 675–680. <https://doi.org/10.1039/C0SC00381F>.
- (73) Tonhauser, C.; Natalello, A.; Löwe, H.; Frey, H. Microflow Technology in Polymer Synthesis. *Macromolecules* **2012**, *45* (24), 9551–9570. https://doi.org/10.1021/MA301671X/ASSET/IMAGES/LARGE/MA-2012-01671X_0032.JPEG.
- (74) Weiss, K.; Khoshgoftaar, T. M.; Wang, D. D. A Survey of Transfer Learning. *J. Big Data* **2016**, *3* (1), 1–40. <https://doi.org/10.1186/s40537-016-0043-6>.